



Influence of air annealing on the characteristics of spray-deposited TiO₂ thin films and their use as NO₂ gas sensors

RS Madhukeswara¹ · R. Shashidhar² · A. Raghu³ · GS Prakasha⁴

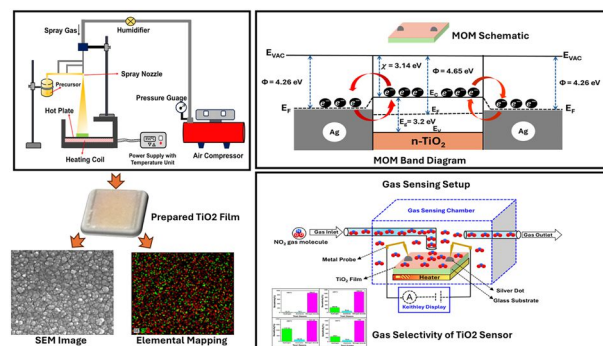
Received: 27 February 2025 / Accepted: 12 August 2025 / Published online: 2 September 2025

© The Author(s), under exclusive licence to Springer Science+Business Media, LLC, part of Springer Nature 2025

Abstract

Titanium dioxide (TiO₂) thin films were deposited at 350 °C on thoroughly cleaned substrates using an economical spray pyrolysis process. The film's structural, morphological, compositional, optical, and electrical properties were examined using XRD, Raman spectroscopy, XPS, FTIR, SEM, EDS, UV-Vis-NIR, and Hall-effect methods. The XRD analysis reveals the anatase nature of the film, with a reduction in peak intensities observed in the sample annealed at 450 °C. The EDX investigation reveals that the film is composed only of Ti and O, which has been confirmed by XPS analysis. FTIR studies confirmed the existence of Ti-O-Ti stretching bonds. The Raman spectra indicate the existence of microstress and anatase phases. SEM images suggest recrystallization during annealing may result in a slight rise in grain size within the crystalline films. The optical study reveals that air annealing is a useful technique to tailor a film's porosity. The Hall effect study indicates the n-type material conductivity of films. Four distinct target gases-nitrogen dioxide (NO₂), carbon dioxide (CO₂), ammonia (NH₃), and hydrogen (H₂) were used to study the gas selectivity of the TiO₂ nanostructured-based metal oxide sensor at various operating temperatures. The sensor exhibits excellent stability, NO₂ gas selectivity, and response. The sensor's optimum operating temperature was determined to be 250 °C and at this temperature, a response time of 53 s and a recovery time of 125 s were observed for a 5 ppm NO₂ gas concentration. The developed sensor may find use in medical and industrial fields.

Graphical abstract



✉ RS Madhukeswara
madhurs52545@gmail.com

¹ Department of Physics, Government College for Women (Autonomous) (affiliated to Mandya University), Mandya 571401, India

² Department of Physics, J S S Academy of Technical Education (affiliated to Visvesvaraya Technological University), Bangalore 560060, India

³ Department of Physics, Government College (Autonomous) (affiliated to Mandya University), Mandya 571401, India

⁴ Department of Physics, Global Academy of Technology (affiliated to Visvesvaraya Technological University), Bangalore 560098, India

Keywords Spray pyrolysis · TiO₂ · Ambient air annealing · Metal oxide gas sensor · NO₂

Highlights

- Isochronal air annealing enhances the structural, morphological, and optical properties of spray-deposited TiO₂ films.
- The proposed sensor demonstrates remarkable selectivity for NO₂ in comparison to H₂ and NH₃ gases.
- The sensor's response is significantly influenced by the nature and concentration of the target gas.
- The optimum operating temperature and concentration for NO₂ gas are 250 °C and 5 ppm, respectively.
- The spray-pyrolyzed TiO₂ nanostructured sensor device offers a viable platform for high-performance NO₂ detection in medical and industrial applications.

1 Introduction

Automobile emissions, industrial activity, and agricultural practices are significant sources of atmospheric pollution, which has consistently risen since the early twentieth century. Urban and rural areas see sporadic increases in air pollutants such as ozone (O₃), nitrogen dioxide (NO₂), and carbon monoxide (CO). Extended exposure to low concentrations of NO₂ can lead to respiratory problems, chest pain, and chronic pulmonary diseases, while environmentally, it contributes to acid rain through the formation of nitric acid. The World Health Organization (WHO) recognizes NO₂ as a significant air contaminant due to its substantial health impacts. The 2021 World Health Organization Global Air Quality Guidelines specify that nitrogen dioxide (NO₂) exposure should not surpass an annual mean concentration of 10 µg m⁻³ or a 24-h mean concentration of 25 µg m⁻³.

In this context, NO₂ sensors are crucial for real-time air quality monitoring by measuring nitrogen dioxide levels, enabling pollution evaluation, assuring regulatory adherence, and protecting public health and the environment. Common materials employed for NO₂ detection are metal oxides, including tin dioxide (SnO₂) [1], zinc oxide (ZnO) [2], tungsten trioxide (WO₃) [3], copper oxide (CuO) [4], titanium dioxide (TiO₂) [5], and graphene [6]. The above studies suggest titanium dioxide (TiO₂) is a suitable sensing material for NO₂ gas detection.

Titanium dioxide (TiO₂)-based sensors are extensively utilized for the detection of nitrogen dioxide (NO₂) gas, owing to the many essential characteristics of TiO₂ that render them particularly effective for gas sensing applications [5]. TiO₂ exhibits exceptional sensitivity to NO₂ gas owing to the strong interaction between the gas molecules and the TiO₂ surface, particularly in its nanostructured variants. TiO₂ is a wide-bandgap semiconductor, and its electrical resistance varies markedly with the adsorption of NO₂ molecules. This feature enables the measurement of NO₂ gas concentrations via quantifiable alterations in electrical conductivity. The NO₂ molecules can adsorb electrons of TiO₂ surface. This interaction modifies the charge carrier density in TiO₂ film,

facilitating effective detection. TiO₂ exhibits thermal stability at elevated temperatures, enabling its functionality in extreme conditions where NO₂ is commonly present, such as industrial environments or automotive exhaust systems. Titanium dioxide (TiO₂) may be synthesized into various nanostructures, including nanoparticles, nanorods, and nanotubes, which offer a high surface area-to-volume ratio, hence improving gas adsorption and sensor efficacy [5]. TiO₂ sensors can be optimized for selective detection of NO₂ among other gases through suitable doping or surface modifications, hence improving their performance in mixed-gas environments [7]. The characteristics of TiO₂-based sensors render them very effective, reliable, and versatile for NO₂ gas detection in environmental monitoring, industrial operations, and automotive systems. Israa Akram Abbas et al. have reported that the fabricated air annealed TiO₂-based sensors not only had better NO₂ gas sensitivity but also exhibited reproducible and stable results [8].

Diverse synthesis methodologies, including hydrothermal [9], chemical bath deposition (CBD) [10], physical vapor deposition [11], ultrasonic dispersion [12], and spray pyrolysis [13], have been utilized to fabricate TiO₂ thin films. Spray pyrolysis is a versatile and widely used technique for the deposition of titanium dioxide films, presenting many benefits for a range of applications [14]. It produces uniform and smooth TiO₂ coatings across large areas [15], ensuring consistent performance essential for sensors, photovoltaics, and photocatalysts. The method is exceptionally scalable, rendering it appropriate for industrial-scale production [16]. Spray pyrolysis enables systematic regulation of film composition by changing the precursor solution. Critical factors like substrate temperature [17], precursor concentration, and spray rate can be adjusted to enhance the thickness, crystallinity, porosity, and functional characteristics of the TiO₂ films. The process is suitable with several substrates, including glass, metals, ceramics, and flexible polymers; hence increasing its flexibility.

In the present study, by employing a simple, cost-effective, homemade spray pyrolysis technique, TiO₂ thin films were deposited. The objective of this study is to explore the effects of air annealing temperature on the

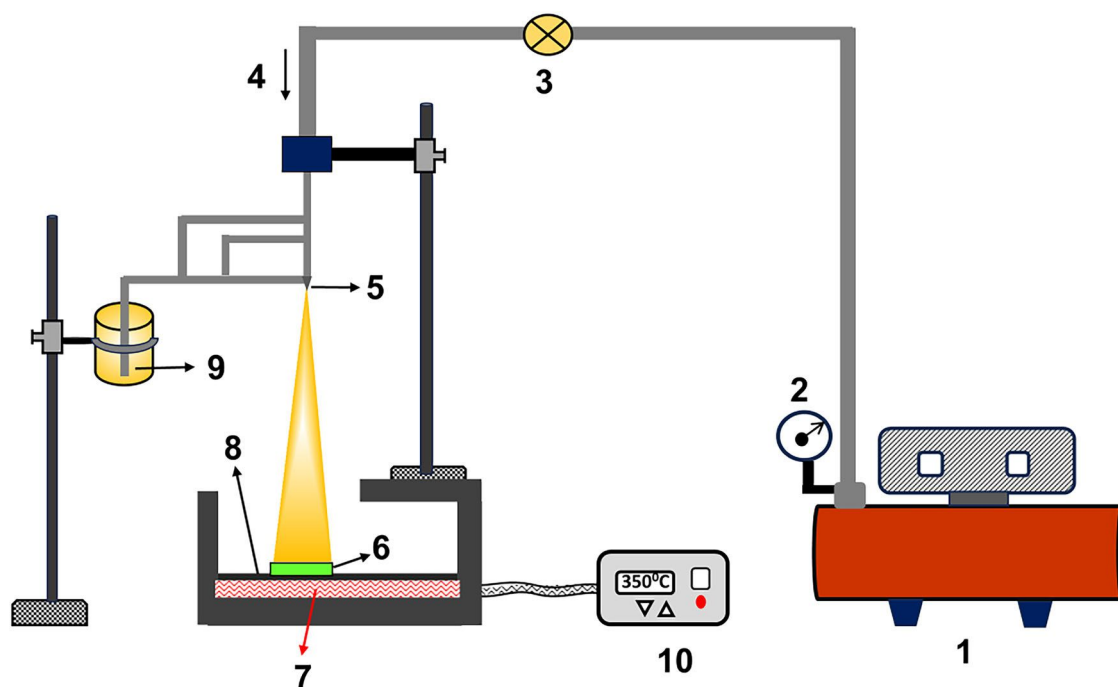


Fig. 1 Schematic diagram of homemade spray pyrolysis set up Inset. 1. Air Compressor, 2. Pressure Gauge, 3. Humidifier, 4. Gas Inlet, 5. Spray Nozzle, 6. Substrate, 7. Heater, 8. Hot Plate, 9. Precursor Solution, 10. Power Supply with Temperature Unit

structural, morphological, optical, and electrical properties of nanostructured TiO_2 thin films. Then utilize optimized TiO_2 thin films to fabricate NO_2 gas sensor and study its performance as a function of gas concentration and operating temperature.

2 Materials and methods

2.1 Materials used

The precursor solution of 75 ml was prepared by combining titanium isopropoxide (Sigma Aldrich, 99.5% purity), acetylacetone (Sigma Aldrich), and ethanol (Sigma Aldrich) at a volumetric ratio of 1:1.5:22.5 (3 ml + 4.5 ml + 67.5 ml). The prepared solution's pH was found to be 6.4. The quartz and glass substrates, having an area of 1 cm^2 , were pre-cleaned using acetone, chromic acid, and deionized water. The p-type Si substrates of resistivity 5–10 $\Omega \text{ cm}$ and thickness 525 ± 25 microns with (100) orientation of area 1 cm^2 were pre-cleaned utilizing the RCA-1 and RCA-2 techniques [18, 19]. The RCA technique refers to a widely-used semiconductor cleaning process to remove organic, inorganic, and particle impurities.

2.2 Experimental methods

A homemade spray pyrolysis setup is employed for the deposition of TiO_2 film on various pre-cleaned substrates.

The schematic representation of the homemade spray pyrolysis setup used in the current work is shown in Fig. 1. The substrate and spray nozzle were positioned at a specified distance of 30 cm, with the air pressure was adjusted to 4.2 kg cm^{-2} . The substrate temperature was maintained at a constant $350 \text{ }^\circ\text{C}$ throughout the deposition processes. To achieve TiO_2 film of desired thickness it was planned to perform spray for a time of 180 s, in 36 cycles, at an optimized rate of 5 s spray per cycle followed by a 30 s pause cycle, to sustain a substrate temperature of $350 \text{ }^\circ\text{C}$. Different substrates, such as silicon, quartz, and glass of 1 cm^2 area, were employed for spray deposition at the specified conditions.

The TiO_2 thin films, prepared on various substrates, underwent air annealing for one hour at specified temperatures of $400 \text{ }^\circ\text{C}$, $450 \text{ }^\circ\text{C}$, and $500 \text{ }^\circ\text{C}$ to analyse the influence of annealing on their microstructural, morphological, compositional, optical, and electrical properties. The optimal annealing temperature range for the synthesis of pure and stable anatase TiO_2 films is 400 to $500 \text{ }^\circ\text{C}$; hence, this range was used for annealing in the present study [20]. The TiO_2 films deposited on Si substrates were utilized for XRD, Raman, FTIR, SEM, XPS, and EDS characterizations due to their compliance with these methodologies. Silicon substrates are better for X-ray diffraction (XRD) studies than glass because silicon's crystal structure gives clear, sharp peaks, which makes it easier to identify the sample's peaks, while glass is not structured and creates wide, less useful patterns.

Silicon substrates are chosen for Scanning Electron Microscopy (SEM) and Energy-Dispersive X-ray Spectroscopy (EDS) studies instead of glass because they conduct electricity and heat better, are stronger, and do not react with chemicals, which helps reduce issues like sample charging, overheating, and contamination.

The TiO₂ films deposited on quartz substrates were utilized for optical studies over glass due to their superior optical properties, particularly high UV transmission, exceptional thermal and chemical resistance, and high purity, making them ideal for applications requiring precise light transmission and stability. The TiO₂ films deposited on a glass substrates were employed for electrical studies, as glass is an insulator, making it suitable for measuring the electrical properties of thin films without substrate interference. Furthermore, the TiO₂ film annealed at 500 °C on a glass substrate was employed for gas response studies. Hereafter, the as-deposited TiO₂ film will be referred to as T1, while those subjected to air annealing at 400 °C, 450 °C, and 500 °C will be referred to as T2, T3, and T4, respectively.

Structural analysis of both the as-prepared and air-annealed TiO₂ thin films was carried out using an X-ray diffractometer (Rigaku Smart Lab XRD) with a Cu K α X-ray source, a 2 θ scan range of 20° to 80°, a scan speed of 2.4° per minute, and a step size of 0.01°. An X-ray photoelectron spectrometer (Kratos-Axis Ultra DLD) equipped with a monochromatic Al K α source (1486.6 eV) together with a charge neutralizer to prevent static charge accumulation was used for XPS research. The Perkin Elmer-Frontier MIR with a spectral range 400–4000 cm⁻¹ and a spectral resolution of 1 cm⁻¹ was used for the FTIR investigation. The Raman Spectrometer (Horiba-Lab RAM HR), employing a 532 nm laser, was used for Raman study, which involves a spectral resolution of 0.3 cm⁻¹ per pixel and a scan range of 60 to 1200 cm⁻¹. For the optical investigation, a UV-3600 MPC-3100 UV-Vis-NIR spectrometer of a scan range 200 nm to 1200 nm with 1 nm increments was employed. The EDS investigation, which offers elemental characterization of the samples, was conducted using MIRA 3 (FESEM) and Quantax 200 (EDS), along with Evactron XEI (plasma cleaner) (TESCAN and Bruker). For electrical studies, DC Probe Station-2 [Semiconductor Device Analyzer B1500A (SDA) with Micro Tech PM5] and a Polytronic HEM-150 electromagnet producing a 1 T magnetic field were utilized. The TiO₂ sensor's gas-detecting response was studied using a gas-sensing calibration setup at IISc in Bangalore, India. The procedure used for studying the target gas response is explained below.

The sensor response quantifies the proportionate rise (or fall) of the sensor output signal in the presence of a certain

concentration of target gas when compared to pure synthetic air. Synthetic air refers to a man-made gas combination that has a predetermined proportion of 80% nitrogen and 20% oxygen so that it closely mimics the composition of natural air. Gas sensors are calibrated using synthetic air to ensure precise measurements. Synthetic gas of 500 standard cubic centimetres per minute (sccm) is purged onto the sensor at the working temperature until the baseline stabilizes. Once a stable baseline is established, the sensor is subjected to a purging process using a target gas, which can be either an oxidizing or reducing gas, with a prescribed concentration (a target gas concentration of 5 ppm is utilized in the current study) until sensor resistance reaches a stable state. Subsequently, the target gas is deactivated, and the synthetic gas of 500 sccm is once again purged till the sensor recovers its normal operation and its resistance aligns with the baseline value. The same process is iterated for the selected target gases, maintaining the uniform gas concentration at various operating temperatures. This study aims to estimate the ideal operating temperature and the target gas with the maximum sensor response. For the ppm cycle, the target gas that exhibits a strong response at an optimal temperature is taken into account. The sensor response for the selected target gas is examined by gradually increasing its concentration in the range of 1–5 ppm, with increments of 1 ppm. The sensor's stability is assessed by repeating the ppm cycle after 30 days using the selective target gas, NO₂ at an optimal temperature of 250 °C.

The gas sensor typically produces an electrical output signal upon exposure to a test gas. The interaction with gas molecules alters the electrical properties of the sensor material, referred to as the sensor's response *S*. When the oxidizing target gas reacts with the n-type metal oxide gas sensor (e.g., TiO₂), the gas molecules are going to drain the electrons by chemically reacting with the sensor material; as a result, the sensor's resistance increases. The gas response *S* is calculated using the relation given below [21].

$$S = (R_g - R_a)/R_a \quad (1)$$

where *R_a* and *R_g* denote the equilibrium values of sensor resistances in the synthetic air and target gas, respectively.

When the reducing target gas interacts with the n-type metal oxide gas sensor, the gas molecules release electrons by chemically reacting with the sensor material; as a result, the sensor's resistance decreases. The gas response *S* is calculated using the relation given below [21].

$$S = (R_a - R_g)/R_a \quad (2)$$

In general, the gas response in percentage is calculated using the relation given below.

$$S(\%) = |(R_g - R_a)/R_a| \times 100 \quad (3)$$

3 Results and discussions

3.1 XRD analysis of TiO₂ films

The structural characteristics of the spray-deposited TiO₂ films were examined using X-ray diffraction (XRD), as shown in Fig. 2. The primary peaks were found at $2\theta = 25^\circ$, 48.1° , 55.2° , 62.8° , 70.6° and 75.37° corresponding to the diffraction planes (101), (200), (211), (213), (220) and (107) respectively, indicating a tetragonal crystal structure in the anatase phase, as confirmed by JCPDS cards [00-001-0562, 96-900-9087]. Table 1 presents the estimated structural parameters obtained from the XRD spectrum.

This structural analysis was contrasted with previous research findings [22–24]. Previous studies have described the anatase-rutile mixed phase; however, our research identified the anatase phase as predominant, suggesting that the primary pressure influences the orientation of crystalline structure development. This may be associated with the fact that the anatase phase possesses reduced surface energy, elevated cohesive energy, and diminished bulk modulus [25, 26]. Consequently, this outcome can be exemplified by the presence of anatase as a stable phase in the low-pressure, low-temperature area of the P-T diagram [27]. The observed drop in peak intensity beyond 400 °C may be due

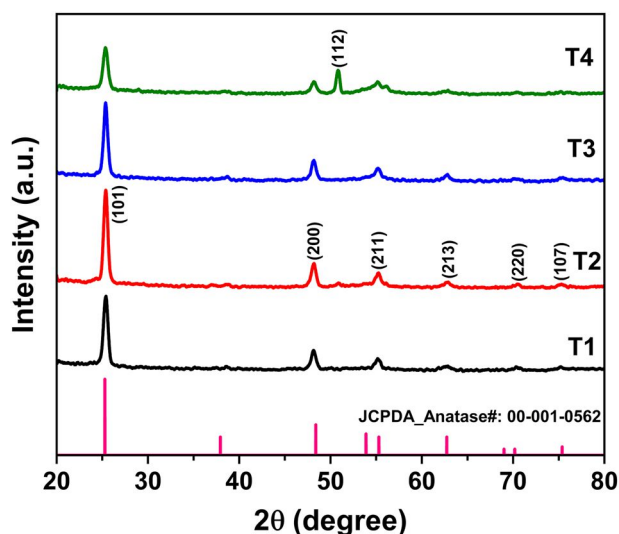


Fig. 2 XRD patterns of spray deposited TiO₂ films

Table 1 Estimated structural parameters of as deposited and air annealed TiO₂ films for the most intense (101) XRD peak

Sample	2θ degree	FWHM(β)	Crystallite size(D) nm	Interplanar distance(d) nm	Dislocation density(δ) nm ⁻²	Microstrain (ε)	Crystallinity %
T1	25.37	0.5897	14.1732	0.3507	0.0050	0.0212	44.77
T2	25.37	0.5392	15.5006	0.3507	0.0042	0.0194	98.69
T3	25.37	0.5461	15.3004	0.3508	0.0043	0.0202	79.96
T4	25.35	0.6181	13.5025	0.3511	0.0055	0.0248	90.20

to the development of internal stress in the films [28]. The newly observed peak at $2\theta = 51^\circ$ on p-type (100) silicon substrate corresponds to the (112) plane of SiO₂ [29].

Table 1 displays the calculated structural parameters of spray-deposited TiO₂ thin films in relation to annealing temperatures. The analysis indicates that the interplanar spacing slightly increases with temperature. The dislocation density and microstrain initially decrease, reach a minimum, and then increase; however, both crystallite size and crystallinity were found to be at their maximum at 400 °C. The rise in crystallinity for the T4 sample may result from the emergence of new peaks in the T4 spectra, whereas the reduction in crystallite size for the most prominent peak (101) of T4 is attributed to elongation stress, leading to an increase in the FWHM (β) value, potentially related to the formation of new peaks.

3.2 XPS analysis of TiO₂ films

Figure 3 illustrates the XPS spectra of both as-deposited and air-annealed TiO₂ films across the whole binding energy range, revealing the typical peaks of C 1 s, O 1 s, and Ti 2p. It is found that the increase in temperature results in a corresponding increase in the intensities of the XPS peaks.

The increment of peak intensity with temperature may be attributed to the growth of TiO₂ crystals, resulting in a more ordered and crystalline structure. TiO₂ can exist in different phases, such as anatase, rutile, and brookite, and annealing can influence the phase transformation and the relative abundance of each phase [30]. Annealing can also lead to changes in the surface morphology and composition of TiO₂, potentially affecting the intensity of XPS peaks [31].

The Ti 2p spectra (inset display in Fig. 3) reveal two prominent symmetric peaks at approximately 464.3 ± 0.2 eV and 458.5 ± 0.2 eV, corresponding to Ti 2p_{1/2} and Ti 2p_{3/2}, respectively. The 5.8 eV peak separation observed in the Ti 2p doublet aligns well with the energy documented for anatase phase TiO₂ nanoparticles [32, 33].

During air annealing, the binding energies of Ti 2p were shifted towards 459.5 ± 0.2 eV for Ti 2p_{3/2} and towards 465.2 ± 0.2 eV for Ti 2p_{1/2}, in accordance with other reports [34]. This transition may result from the reduction of Ti⁴⁺ ions to Ti³⁺ deficient states, typically associated with a loss of oxygen from the TiO₂ surface.

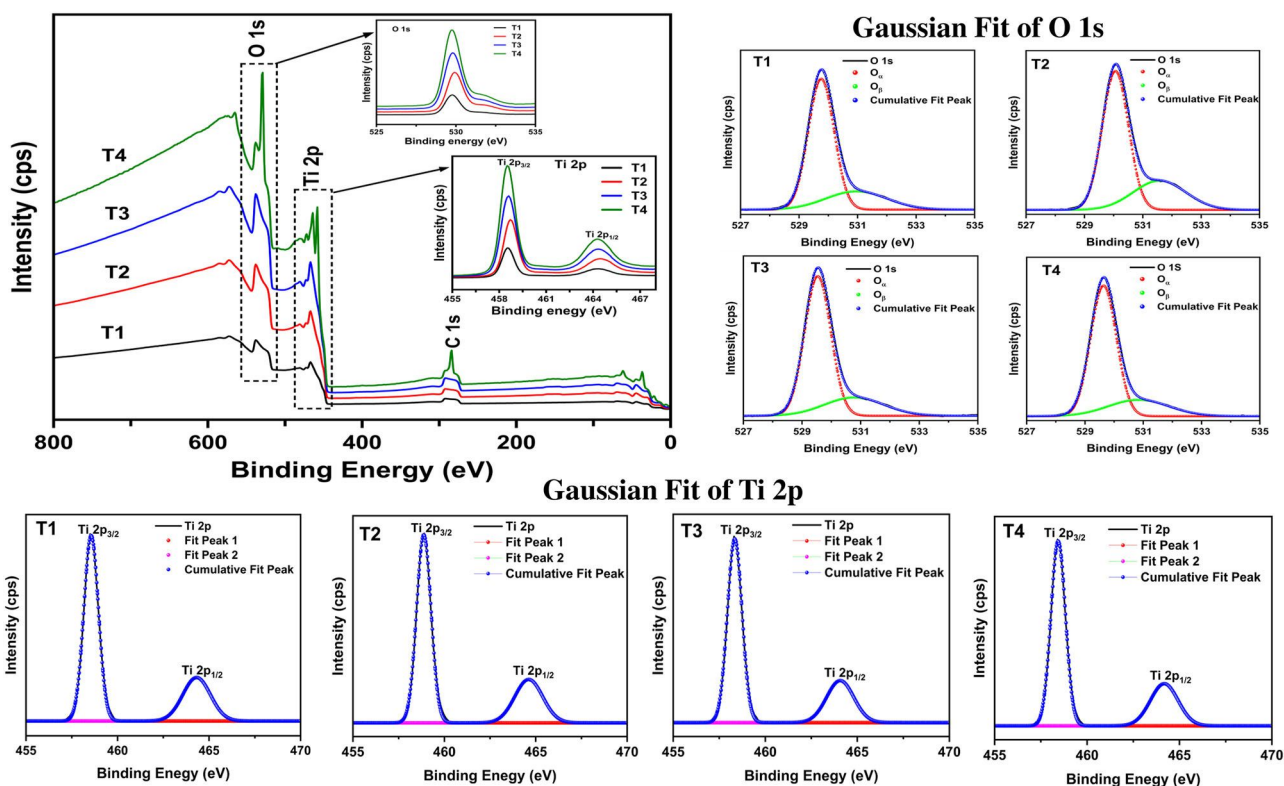


Fig. 3 XPS spectra of spray deposited TiO_2 films

A secondary inset in Fig. 3 displays a magnified O 1s XPS spectrum. Two oxygen chemical species were identified in the as-deposited and air-annealed TiO_2 films. The primary peak of TiO_2 lattice oxygen (O_α) accounted for the reduced binding energy (BE) at around 529.7 ± 0.2 eV, while the surface weakly bound (or adsorbed) oxygen (OH and molecular O_2 species- O_β) was indicated by the additional peak at 532.8 ± 0.2 eV [35].

All films exhibited a C 1s peak with a binding energy of 284.6 eV. The presence of C 1s is linked to organic surface contamination due to the sample's exposure to air [20].

In the present study, TiO_2 -XPS analysis reveals characteristic indication of surface oxygen vacancies as a result of peak shift in the O 1s spectrum and also the existence of Ti^{3+} in the Ti 2p spectrum for films annealed at 500°C (T4). The O 1s peak intensity is seen to be maximum at this temperature [36]. This may be one of the causes for better gas-sensing performance of T4 gas sensor [37].

3.3 FTIR analysis of TiO_2 films

The typical FTIR spectra of the air-annealed and as-deposited TiO_2 films are displayed in Fig. 4. This shows that the primary bands were detected around $3400\text{--}3800\text{ cm}^{-1}$ and at 2963 , 2322 , 1454 , and 1106 cm^{-1} respectively [38–40]. The stretching vibrations of hydroxyl (O-H) groups were observed

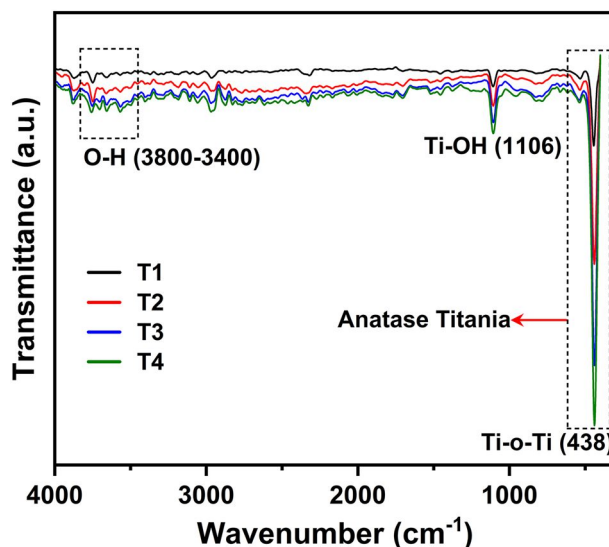


Fig. 4 FTIR spectra of spray deposited TiO_2 films. The region marked within the dashed rectangles were explained in the text

at 3400 cm^{-1} . The bending vibrations of coordinated H_2O and Ti-OH produced a peak at 1106 cm^{-1} . It is commonly observed in infrared spectroscopy studies of titanium-containing materials, particularly in the context of Ti-O bonds and associated water molecules. Furthermore, when the film was annealed, the results showed a dominant feature that was centered around 438 cm^{-1} , which is

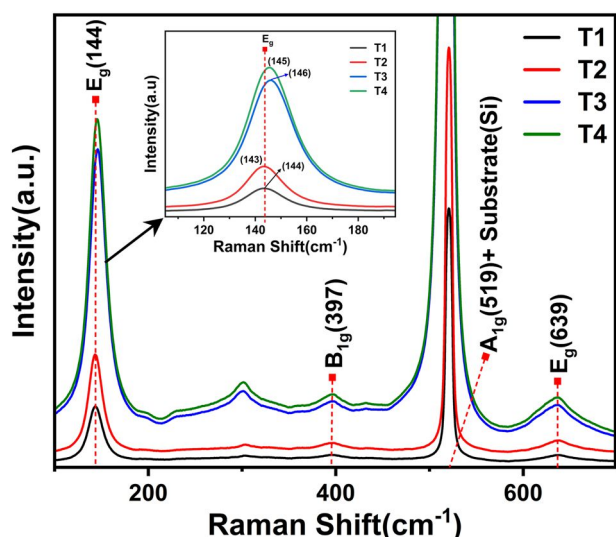


Fig. 5 Raman spectra of spray deposited TiO₂ films

typical of the anatase [41]. For the sample that was air-annealed at 350 °C, this peak was extremely weak. When the sample was annealed at 500 °C in air, peak became stronger and more pointed in accordance with the published literature [42].

3.4 Raman spectral analysis of TiO₂ films

Figure 5 displayed the Raman spectra of as deposited and air annealed spray-deposited TiO₂ films. The Raman modes at 144 cm⁻¹, 397 cm⁻¹, 519 cm⁻¹, and 639 cm⁻¹ validated the purity of anatase TiO₂ and no brookite phase was observed. The anatase phase at 144 cm⁻¹ exhibits a peak in all the TiO₂ films. It emerged that as the annealing temperature was increased, so did the intensities of the anatase phase peaks. However, as the annealing temperature increased, the anatase phase peak positions shifted from 144 cm⁻¹ to 146 cm⁻¹ [43]. Raman spectral investigations reveal the presence of six active Raman scattering bands in anatase-TiO₂: 144 cm⁻¹ (E_g), 399 cm⁻¹ (B_{1g}), 513 cm⁻¹ (A_{1g}), 519 cm⁻¹ (B_{1g}), and 639 cm⁻¹ (E_g) [44]. One minor peak at 302 cm⁻¹ was due to the Si-Si stretching mode of the substrate, and another strong peak at 521 cm⁻¹ is superposed with two TiO₂ peaks around 519 cm⁻¹ again demonstrating the Si-Si stretching mode of the substrate [45]. The intensity of the band shows that the crystalline TiO₂ anatase structure is on the Si surface after oxidation.

3.5 SEM analysis of TiO₂ films

Fig. 6 displays the surface morphology of the TiO₂ films. Table 2 reveals that recrystallization due to annealing leads to a considerable increase in grain size from 41.91 nm to 49.13 nm. Conversely, it seemed as though the surface

roughness increased monotonically as the annealing temperature was increased. The grains became more crystalline as the annealing temperature increased. This agrees with the XRD results, which indicated that elevating the annealing temperature increased the crystallinity of the films, as previously observed [46].

3.6 EDS analysis of TiO₂ films

To test the composition of the titanium dioxide film, an energy dispersive spectrometer (EDS) is used. Figures 7 and 8 depict the EDS spectra and elemental mapping of as-deposited and air annealed TiO₂ films. Table 3 presents an EDS analysis of the titanium dioxide films, confirming the presence of the major elements such as oxygen and titanium. No other contaminants were found in the films. The coexistence of native oxide in SiO₂ on silicon substrates may cause excesses of oxygen weight% in Table 3 of TiO₂ films [47]. The elemental mapping shows a homogenous distribution of titanium within the substrate, as well as the presence of oxygen in Fig. 8.

3.7 Optical properties of TiO₂ films

The optical analysis was conducted on all the TiO₂ films using a UV-Vis-NIR spectrophotometer in a wavelength range of 200-1200 nm. Figures 9a and b display the absorbance and transmittance spectra, while Fig. 9c shows the Tauc's plots of the as-deposited and air-annealed TiO₂ films. The absorbance spectra show a slight red shift of absorption edge as a result of variation of crystallite size with relation to temperature. The absorbance has been found to be higher in the ultraviolet portion of the spectrum. The transmittance spectra reveal that transmittance increases with air annealing beyond 300 nm. This may be due to an increase in film porosity.

Table 4 provides the computed optical parameters for as-deposited (T1) and air-annealed (T2, T3, T4) TiO₂ films. The optical investigations revealed that both the film thickness and the optical indirect band gap of the TiO₂ decreased after air annealing. The grain densification with annealing may be responsible for the decrease in the film thickness [48]. The residual stress due to annealing on the film can also account for the thickness variance [49]. This work found that a decrease in film thickness led to a consistent increase in UV region absorption. This variance was observed to affect hydrophilic properties and hence the self-cleaning properties of glass [50]. The SEM histogram analysis clearly shows an increase in grain size with annealing temperature. This variation may be responsible for the decrease in the film's optical band gap [51].

Table 5 presents the estimated parameters that outline the optical properties of TiO₂ films, which include refractive

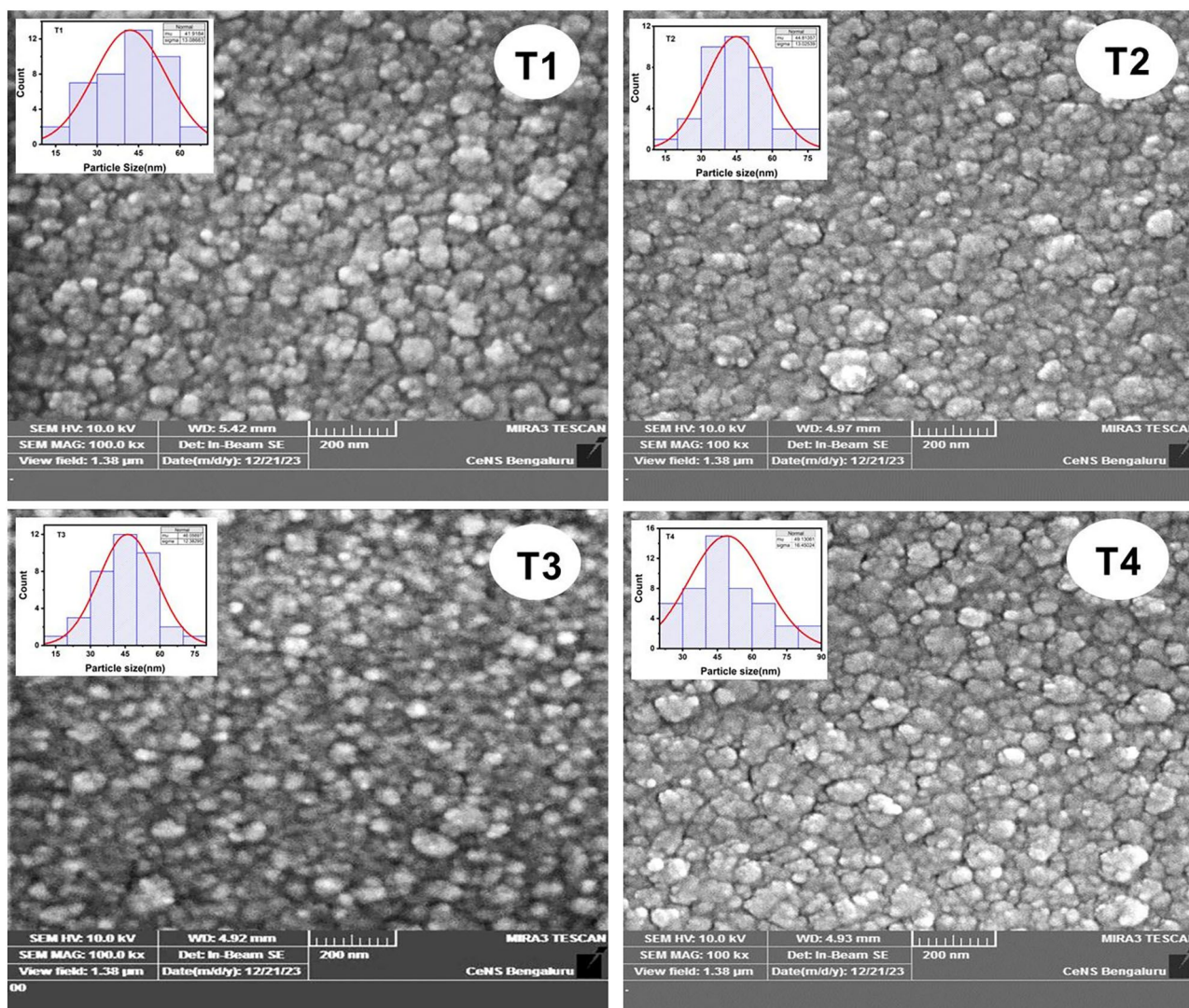


Fig. 6 SEM images of spray deposited TiO₂ films

Table 2 Estimated particle size from SEM Histogram of TiO₂ films

Sample	Grain size (nm)
T1	41.91
T2	44.81
T3	46.05
T4	49.13

index (n), porosity (ϕ), extinction coefficient (k), optical susceptibility (χ), optical conductivity (σ), packing density (p), real part of the dielectric function (ϵ_r), and imaginary part of the dielectric function (ϵ_i). The data were gathered using UV-Vis transmittance data at 600 nm. With the film air annealing, the porosity was found to increase, which could be related to the formation of smaller crystals inside the film. However, the reduction in film thickness resulted in a reduced refractive index, optical susceptibility, packing

density, and real part of the dielectric constant, thereby increasing the material density within the film. At 400 °C, the extinction coefficient, optical conductivity, and imaginary part of the dielectric constant begin to decrease. It turns out that the film, which is air-annealed at 500 °C, has the maximum porosity. Highly porous films may be utilized as gas sensors [52, 53]. The films with higher porosity will improve gas sensing due to their ability to facilitate the diffusion of reaction gases in and out of the film. This enhances the sensor's response and reduces its recovery time [54].

3.8 Electrical studies of TiO₂ films

Table 6 shows the electrical parameters of as deposited, and air annealed TiO₂ films. To estimate film resistivity (ρ), sheet charge concentration (n_s), bulk charge concentration

(n_b), and mobility of charge carriers (μ), the below mentioned equations were employed.

$$\rho = R_s \times t \quad (4)$$

$$n_s = 1/(R_H \times e) \quad (5)$$

$$n_b = n_s/t \quad (6)$$

$$\mu = 1/(R_s \times n_s \times e) \quad (7)$$

Table 3 EDS Analysis of TiO₂ films

Sample	Elements	Weight %	Atomic %	Ti:O Ratio
T1	Oxygen	57.32	80.08	0.25
	Titanium	42.68	19.92	
T2	Oxygen	59.87	81.7	0.22
	Titanium	40.13	18.3	
T3	Oxygen	56.79	79.73	0.25
	Titanium	43.21	20.27	
T4	Oxygen	60.08	81.83	0.22
	Titanium	39.92	18.17	

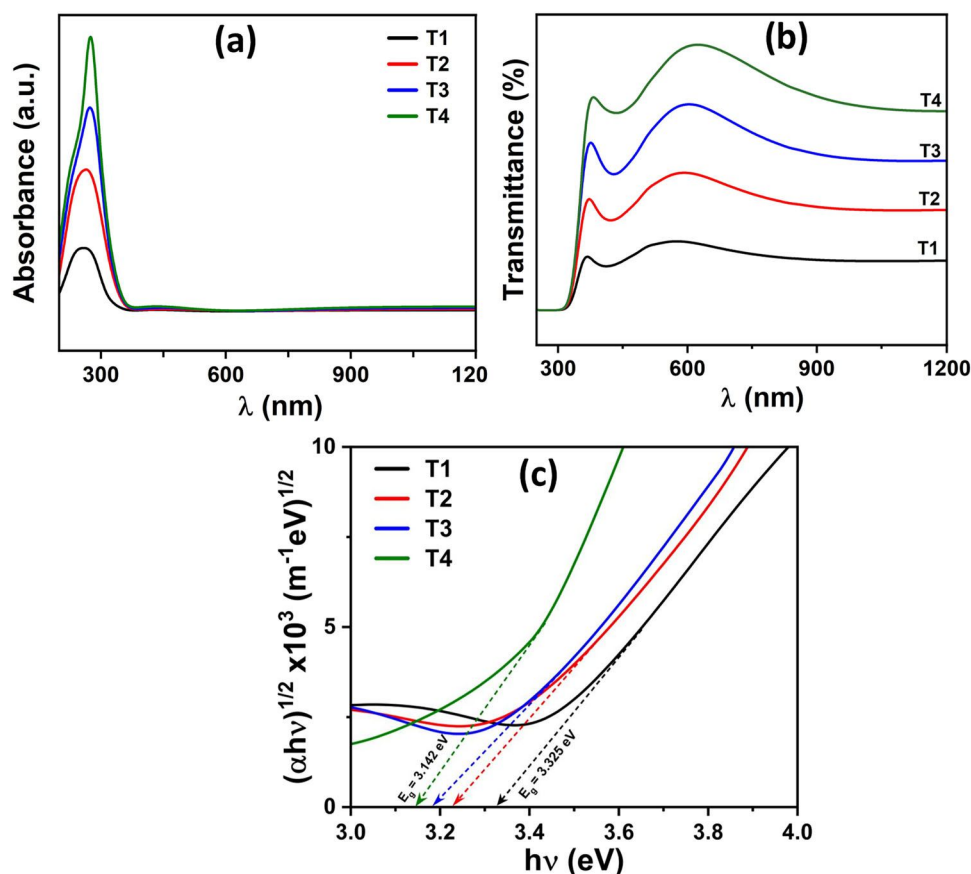
where R_s , t , R_H , and e are sheet resistance, film thickness, Hall coefficient, and charge of the electron, respectively.

The Hall effect studies show that all the films possess n-type conductivity. Both mobility and film thickness were found to decrease with temperature. The mobility due to charge carriers can be further changed by UV light irradiation, and the films may be further used for photocatalysis also [55]. At 400 °C, sheet resistance, resistivity, and Hall voltage were observed to be high. However, at 450 °C, the bulk electron concentration was high due to a minimal Hall coefficient. Doping can further reduce the electrical characteristics, such as sheet resistance, of TiO₂ films [56, 57].

4 Gas sensing studies

Out of the four TiO₂ films deposited on a glass substrate, the T4 film (air annealed at 500 °C) is chosen for gas sensing due to its distinctive characteristics resulting from air annealing. The T4 sample exhibited a combination of reduced crystal size, thickness, energy gap, and packing density, alongside enhanced crystal quality, porosity, flaws, stress, and grain size. The amalgamation of these qualities, coupled with variations in oxygen levels, porosity, optical conductivity, imaginary dielectric constant, and sheet

Fig. 9 **a** Absorbance spectra, **b** Transmittance spectra and **c** Tauc plot of spray deposited TiO₂ films



resistance, enable the film to function effectively as a gas sensor [58].

TiO₂ films annealed at 500 °C often exhibit improved sensing response, likely due to changes in crystal structure [23] and morphology (porosity, nano structures) that enhance the material's interaction with target gases [8]. Annealing at higher temperatures promotes grain growth and improved crystallinity, leading to a more ordered and stable material [59].

Hence, the TiO₂ air-annealed film (T4), prepared at 500 °C on a 1 cm² glass substrate, was employed as a metal oxide sensor for the current gas sensing study, owing to its above cited salient features (Tables 1, 2 and 5).

Table 4 Film thickness and optical bandgap of TiO₂ films

Sample	Film Thickness (t) nm	Optical bandgap (E _g) eV
T1	171.88	3.325
T2	158.13	3.226
T3	139.54	3.181
T4	130.45	3.142

Table 5 Estimated optical parameters by of TiO₂ films at 600 nm

Sample	<i>n</i>	Φ (%)	K	χ	σ (x10 ¹³)	p	ε _r	ε _i
T1	2.40	40.5	0.006	0.38	0.69	0.90	5.74	0.03
T2	2.40	40.5	0.002	0.38	0.03	0.90	5.74	0.01
T3	2.35	44.00	0.01	0.36	0.06	0.89	5.52	0.02
T4	2.30	47.69	0.07	0.34	0.77	0.87	5.29	0.31

Table 6 Electrical properties of as deposited (T1) and air annealed (T2, T3, T4) TiO₂ films

Sample	R _s (MΩ)	t (nm)	ρ (Ω m)	V _H (volt)	R _H (m ³ C ⁻¹)	n _s 10 ¹⁶ (m ⁻³)	n 10 ²³ (m ⁻²)	μ 10 ⁻³ (cm ² /V-s)	Material Type
T1	322	171.9	55.36	-0.133	-73.24	-8.5	-4.96	-2.27	n
T2	417	158.1	66.02	-0.203	-29.44	-22	-13.43	-0.71	n
T3	267	139.5	37.26	-0.109	-10.16	-61	-44.07	-0.38	n
T4	313	130.4	40.79	-0.079	-11.61	-54	-41.25	-0.37	n

Table 7 Comparison of the present study with TiO₂ and other metal oxide sensors for NO₂ gas at a concentration of 5 ppm

Sensing Material	Experimental Method	Substrate	Response Time (s)	Recovery Time (s)	Reference
TiO ₂	Spray Pyrolysis	Glass	53	125	Current Work
TiO ₂ NRs	hydrothermal method	FTO-coated glass	114	125	[71]
TiO ₂	Sol-gel route	Quartz substrate	120-180	240-300	[72]
ZnO	Hydrothermal method	Glass	100-120	115-120	[73]
SnO ₂	Sol-gel	Silicon	80	3600	[74]

Two silver (Ag) electrodes were applied to the T4 sample using silver paste to establish an electrical contact, enabling measurement of the sensor's resistance variation during gas exposure. To achieve proper ohmic contact between the silver metal and the oxide surface, the T4 sample was subsequently heated at 60 °C for 30 min. The metallic probes of the sensing unit were designed to contact silver electrodes during gas detection. Consequently, it serves as an economical means of investigating gas sensing without undergoing expensive metallization costs. The gas sensing studies of the TiO₂ sensor was performed using a calibrated gas sensing setup at the CENSE laboratory, IISc Bangalore, India.

Figure 10 illustrates the schematic representation of the gas sensor setup. A metal oxide gas sensor has been placed within a gas-sensing chamber measuring 39 cm × 33 cm × 23 cm. Alica 500 SCCM MFCs regulated the gas flow within the chamber. In contrast, the Keithley 2450 Source Monitor Unit assessed the current traversing the device, while the Eurytherm 2400 Temperature Controller regulated the sensor temperature.

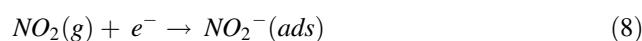
Applying a voltage across the sensor causes current to flow through the circuit. When a target gas is purged into the chamber, the gas molecules interact with the TiO₂ semiconductor oxide surface, which results in the creation of chemical or van der Waals bonds across the gas molecules and the oxide, an adsorbent material. Consequently, there exist two categories of adsorption processes that describe how molecules adhere to the surfaces, namely physisorption and chemisorption. Physisorption is caused by weak van der Waals forces. Chemisorption occurs when the chemical bonds are formed (covalent or ionic). During the purging of oxidizing gas (e.g., CO₂, NO₂) on an n-type

Table 8 Interpretation of the present study in relation to other metal oxide sensors for NO₂ gas sensing

Sensing Material	Experimental Method	Substrate	Testing Range (ppm)	Optimum gas concentration (ppm)	Response Time (s)	Reference
TiO ₂	Spray pyrolysis	Glass	1–5	5	53	Current work
Au: TiO ₂	R F magnetron sputtering	Langasite (LGS)	510–1060	510	10	[75]
TiO ₂	Sol–gel electrospinning technique	IDE	10–130	20	5–17 min	[76]
Cr: TiO ₂	Anodization	Ti–Pt electrode	10–100	25	3–6 min	[77]
TiO ₂	Electrophoretic deposition	Alumina	2–6	6	1.5 min	[62]
TiO ₂	3D heterogeneous integration technology (3DHI)	Si: glass	0.85–4.25	4.25	7	[78]
SnS ₂ / mesoporous TiO ₂	Two-step solvothermal method	Pre etched FTO	10–50	2	194	[79]
SnO ₂	Sol–gel	Silicon	1–20	5	80	[80]

sensing material (e.g., TiO₂), electrons migrate from the sensor surface to the molecules of the adsorbed gas. Consequently, the electron concentration on the sensor surface declines, leading to a decrease in conductivity and an increase in sensor resistance. Conversely, when reducing gas (e.g., H₂, NH₃) is purged on an n-type sensor, electrons transfer from the adsorbed gas molecules to the sensor surface, resulting in an increased conductivity and a subsequent decrease in sensor resistance. Vice versa happens for p-type sensors (e.g., CuO) [60].

Upon interaction with NO₂ gas, TiO₂ films facilitate the adsorption of NO₂ molecules on their surface, resulting in a reduction in resistance due to the establishment of a conductive pathway through electron transfer. The chemical reaction [61, 62] is represented by



By computing the electric current (I) through the film and knowing the voltage V across it, the sensor resistance can be estimated using conventional Ohm's law. As the absolute change in resistance fails to provide any information on the sensitivity of the sensor, the relative change in resistance is determined using an Eq. (3).

When a target gas is purged into the gas sensor chamber, the main mechanism by which the semiconductor or oxide reacts to an oxidizing gas is the modification of the adsorbed oxygen species concentration. Adsorbed oxygen reduces the sensor surface's resistance. Rising electron density on the semiconductor surface further creates Schottky potential barriers at grain boundaries. Oxidizing gases raise the concentration of surface oxygen, thereby increasing the sensor resistance. The varying stability of surface oxygen species across different temperature ranges implies that this process is temperature dependent. Doping the semiconductor with noble metals or other catalytic materials can further modify the conductance temperature profiles, which are ascertained by the distinct optimal oxidation temperatures of the various gases [63]. Therefore, the gas sensor is heated to the optimal oxidation temperature, which increases its gas response (S), as the operating temperature of a sensor determines its gas response.

Figure 11a depicts the schematic diagram of TiO₂ metal sensor. Figure 11b represents the schematic energy-band diagram of the Ag/n-TiO₂/Ag heterostructure. Silver has a Fermi level (E_F) that is lower than the conduction band of n-type titanium dioxide. Electrons in TiO₂ possess higher energy levels compared to those in Ag. Upon contact with the TiO₂ film, electrons transferred from TiO₂ to Ag to equalize the Fermi levels, as n-type TiO₂ possesses a greater abundance of free electrons. This establishes Schottky barriers at both metal-semiconductor interfaces. This energy barrier prevents electron transfer from Ag to TiO₂. Electrons can traverse these barriers when subjected to excitation, such as gas adsorption during gas purging.

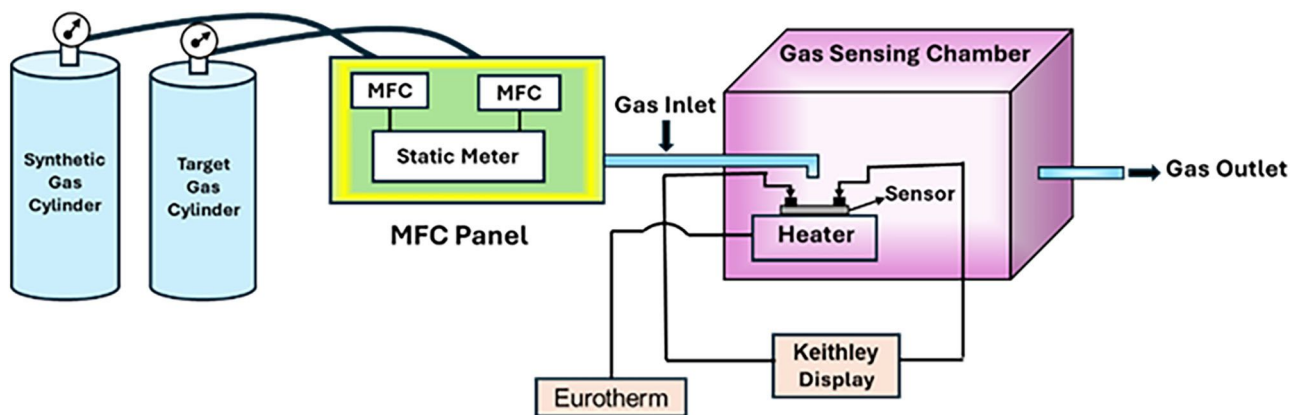


Fig. 10 Schematic diagram of the gas sensing setup

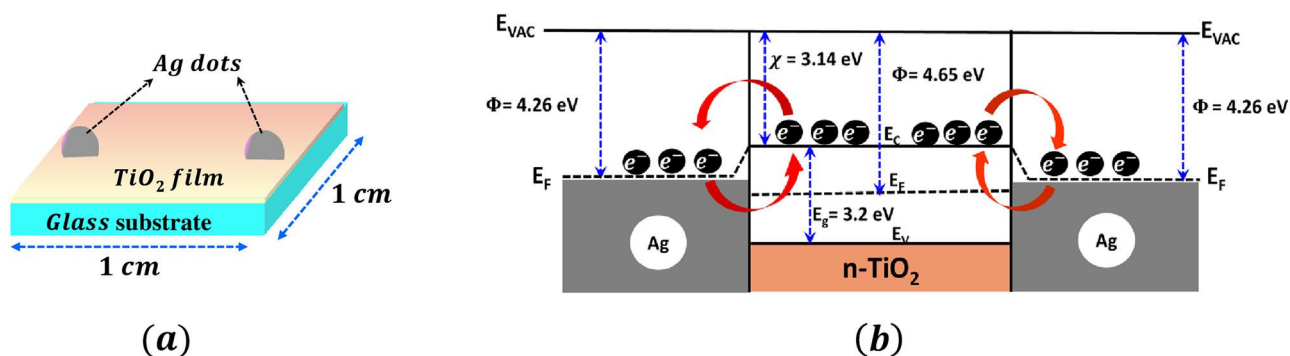


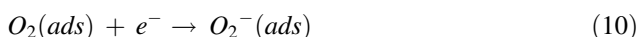
Fig. 11 a Schematic diagram of TiO_2 gas sensor b Schematic energy-band diagram of $\text{Ag}/\text{n-TiO}_2/\text{Ag}$ heterostructure

The gas selectivity of the TiO_2 metal oxide sensor (T4) for a 5-ppm gas concentration was evaluated using two reducing gases, namely hydrogen and ammonia, and two oxidizing gases, namely nitrogen dioxide and carbon dioxide, as target gases at different operating temperatures.

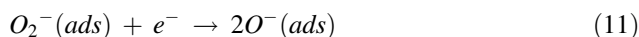
At various operating temperatures, different kinds of oxygen species dominate on the TiO_2 surface, each participating in specific surface reactions with target gases. Before interacting with target gases, oxygen is adsorbed and ionized on the TiO_2 surface. At lower temperatures, the weak adsorption of oxygen species restricts their reactivity, leading to a decreased sensor response. In contrast, at intermediate temperatures, the abundance of O^- species increases surface reactivity, enabling optimal gas sensing performance. The adsorption and transformation of oxygen species on TiO_2 occur under changing temperatures as follows [64, 65]: At below 100 °C temperatures,



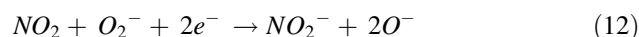
At intermediate temperatures (100–200 °C),



At elevated temperatures (>200 °C),



The NO_2 gas can interact with surface-adsorbed oxygen with the interaction [62],



From room temperature up to 140 °C, the T4 sensor exhibits no response for the target gases. However, upon exposure to target gases at 150 °C, it produces a slight response for H_2 , NH_3 and NO_2 , with the exception of CO_2 . TiO_2 is not inherently sensitive to CO_2 gas for a few reasons: it has a large band gap of 3.2 eV, low affinity and hence poor CO_2 adsorption and activation, and fast recombination of photogenerated electrons and holes [66, 67].

Hence, the gas-selective study was repeated at 200 °C, 250 °C, and 300 °C for the remaining gases (H_2 , NH_3 and NO_2). Figure 12 illustrates the gas response of the T4 sensor for the target gases at various operating temperatures. The selectivity graphs (Fig. 12) indicate that the TiO_2 -based (T4) sensor is more effective in detecting NO_2 gas than H_2

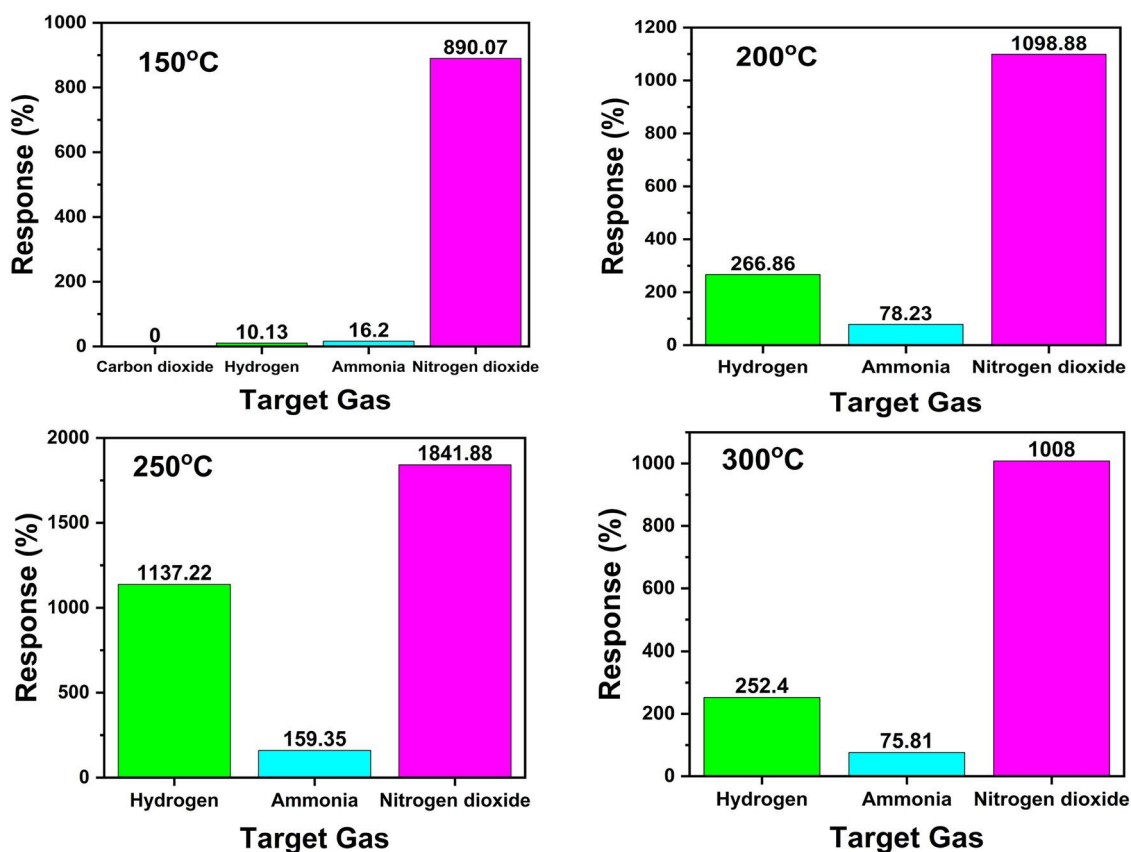


Fig. 12 Gas response of TiO₂ metal oxide sensor (T4) for various target gases as a function of operating temperature

and NH₃ gases at all operating temperatures. The TiO₂ based (T4) sensor shows a gradual increase in gas response with increasing operating temperature and reaches a maximum at 250 °C (Fig. 12) for a 5 ppm NO₂ gas concentration [68]. The possible explanation for the sensor's enhanced response to NO₂ could result from its enhanced surface functionalization with oxygen groups and the subsequent degradation of those groups [69]. Hence, 250 °C is used as the optimum operating temperature for the T4 sensor for further characterization.

The ppm cycle with NO₂ gas for the T4 metal oxide sensor was examined at 250 °C by varying the gas concentration from 1 ppm to 5 ppm. The NO₂ gas was purged for three minutes at each concentration, with a four-minute break between each concentration step. Figure 13a shows the variation of the sensor's resistance with NO₂ gas concentrations. The gas response of the T4 sensor confirms electrical investigation (refer to Table 5), indicating that TiO₂ behaves as an n-type semiconductor, since resistance increases with the entry of oxidizing gas. Figure 13b illustrates the computation of response for each ppm, revealing an increase in response with a surge in gas concentration. The sensor sensitivity, represented by the slope of the response versus NO₂ gas concentration [Fig. 13b],

determined using least squares fitting, and was found to be $314.59 \pm 24.24\%$.

Figure 14 illustrates the variation of response and recovery times of the T4 gas sensor at various NO₂ concentrations. A minimum recovery time of 53 s and a response time of 125 s were observed at 5 ppm. The response and recovery times of a gas sensor might vary based on the gas type, concentration, and the sensor technology employed [70].

The TiO₂-based sensor's (T4) stability was tested by repeating the ppm cycle with NO₂ gas after 30 days at an operating temperature of 250 °C. Figure 15 displays the variation of T4 sensor gas response as a function of time at various gas concentrations both upon fabrication and after a duration of 30 days. The gas response of the TiO₂ metal sensor has reduced marginally after 30 days. The change in the sensor's response for each gas concentration (ppm) was found to be less than 2% after 30 days.

The present study's comparison with existing chemiresistive (Tables 7 and 8) NO₂ sensors indicates that the developed undoped TiO₂ sensor is economically advantageous, which is attributed to the utilization of an affordable glass substrate, a self-constructed spray pyrolysis setup for the film coating, and a single-step electrode development

Fig. 13 **a** Resistance response of TiO₂ metal oxide sensor with NO₂ gas concentration and **b** Response of TiO₂ metal oxide sensor as a function of NO₂ gas concentration (ppm)

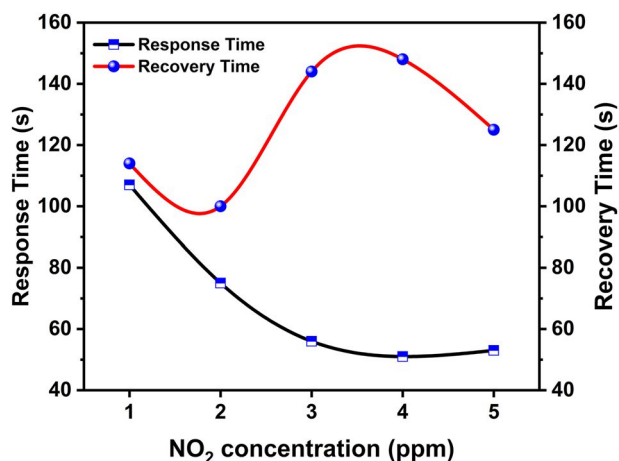
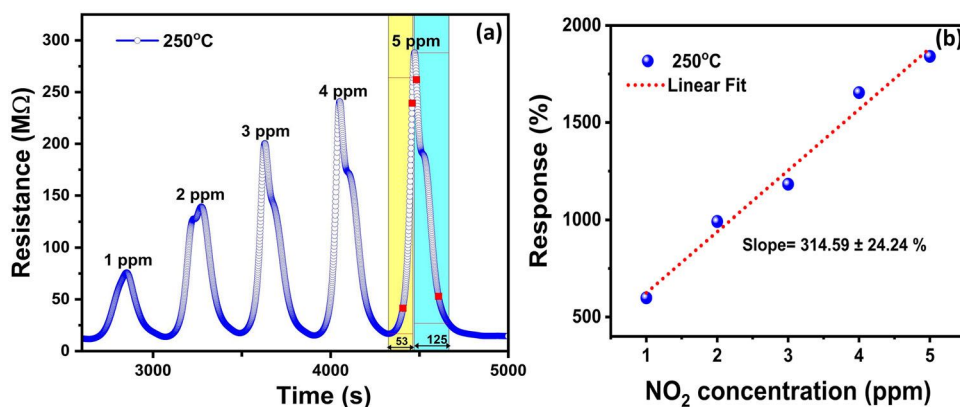


Fig. 14 Response and recovery time of TiO₂ metal oxide sensor with NO₂ gas concentration

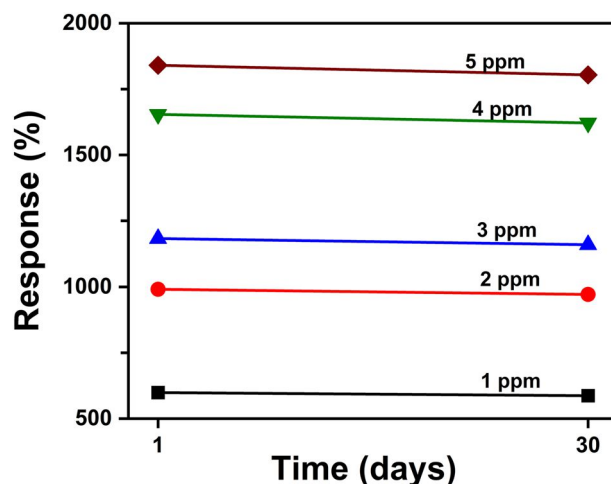


Fig. 15 Stability study of TiO₂ based sensor as a function of time at various NO₂ gas concentration (ppm)

with silver paste. The gas detection of T4 sensor was tested for the gas concentration range from 1 to 5 ppm. The produced TiO₂ metal oxide gas sensor exhibits good selectivity, sensitivity, speed, and stability, despite avoiding the necessity for costly deposition techniques and doping materials such as SnS₂, Au, poisonous chromium, fluorine, and expensive gold and platinum electrodes. However, the speed of the gas sensor can be further improved by adjusting the various spray deposition parameters.

5 Conclusion

The present study utilized a cost-efficient chemical method, specifically spray pyrolysis, to deposit TiO₂ nanostructured films under an ideal condition. The impact of air annealing temperature on the structural, morphological, compositional, optical, and electrical characteristics of TiO₂ films was examined. The XRD study of TiO₂ film indicates an anatase structure and enhanced crystallinity at 400 °C; nevertheless, subsequent annealing results in a further

reduction of crystallite size. XPS and EDS analyses confirm the existence of only titanium and oxygen elements in the films. The SEM histogram indicates an increase in grain size in accordance with the rise in crystallite size with temperature as per XRD. The optical investigations reveal a decrease in the optical band gap with temperature. FTIR and Raman modes confirm the existence of TiO₂ in the film. The UV-Vis-NIR analysis shows that the indirect band gap of TiO₂ thin film decreases with increasing annealing temperature. Hall effect investigations demonstrated the n-type conductivity of the films. The TiO₂ film air-annealed at 500 °C exhibited increased porosity and reduced sheet resistance, prompting us to evaluate its efficacy as a gas sensor. Further the 500 °C annealed film is examined as a metal oxide TiO₂ nanostructured-based gas sensor, and its gas-sensing properties are evaluated with different target gases at varied operating temperatures. The TiO₂ metal oxide sensor shows optimal response towards the oxidizing target NO₂ gas in comparison to reducing hydrogen and ammonia gases at temperatures of 150 °C, 200 °C, 250 °C, and 300 °C. The composition and type of gas impacted the

response and recovery time of the gas sensor. The sensor demonstrates optimal gas response for NO₂ at an operating temperature of 250 °C, with a minimum response time of 53 s and recovery time of 125 s at 5 ppm. Engineered TiO₂ nano-structured metal oxide NO₂ gas sensors may be employed in industrial and medical applications.

Data availability

All data underlying the results is available as part of the article, and no additional resource data is required.

Acknowledgements The authors acknowledge “INUP, Indian Institute of Science, Bangalore” for providing characterization and device testing facilities and “The Central Research Facilities, Center for Nano and Soft Matter Sciences, Bengaluru” for providing characterization facilities. The authors also thank, the Principal, J S S Academy of Technical Education, Bangalore, and the Principal, Government College for Women (Autonomous), Mandya, for their kind support and encouragement.

Author contributions All authors contributed to the study conception and design. Author a* performed material preparation, data collection and analysis. The first draft of the manuscript was written by author a*. Authors b contributed to review, editing, investigation and administration. Authors c contributed to review and editing. Author d contributed to formal analysis. Authors a*, b, c and d read and approved the final manuscript.

Compliance with ethical standards

Conflict of interest The authors declare no competing interests.

References

- Kumar R, Mamta, Kumari R, Singh VN (2023) SnO₂-based NO₂ gas sensor with outstanding sensing performance at room temperature. *Micromachines* 14(4):728. <https://doi.org/10.3390/mi14040728>.
- Patil VL, Vanalakar SA, Patil PS, Kim JH (2017) Fabrication of nanostructured ZnO thin films based NO₂ gas sensor via SILAR technique. *Sens Actuators B Chem* 239:1185–1193. <https://doi.org/10.1016/j.snb.2016.08.130>.
- Sharma S, Tomar M, Puri NK, Gupta V (2014) NO₂ sensing properties of WO₃ thin films deposited by RF-magnetron sputtering. *Conf Pap Sci* 2014(No. 1):683219. <https://doi.org/10.1155/2014/683219> Hindawi Publishing Corporation.
- Navale YH, Navale ST, Chougule MA, Ramgir NS, Patil VB (2021) NO₂ gas sensing properties of heterostructural CuO nanoparticles/ZnO nanorods. *J Mater Sci Mater Electron* 32:18178–18191. <https://doi.org/10.1007/s10854-021-06360-0>.
- Zhu Z, Lin SJ, Wu CH, Wu RJ (2018) Synthesis of TiO₂ nanowires for rapid NO₂ detection. *Sens Actuators A: Phys* 272:288–294. <https://doi.org/10.1016/j.sna.2018.02.006>.
- Soydan G, Ergenc AF, Alpas AT, Solak N (2024) Development of an NO₂ gas sensor based on laser-induced graphene operating at room temperature. *Sensors* 24(10):3217. <https://doi.org/10.3390/s24103217>.
- Gönüllü Y, Rodríguez GCM, Saruhan B, Ürgen M (2012) Improvement of gas sensing performance of TiO₂ towards NO₂ by nano-tubular structuring. *Sens Actuators B: Chem* 169:151–160. <https://doi.org/10.1016/j.snb.2012.04.050>.
- Abbas IA, Hazaa SQ, Salman SH (2021) Employment of Titanium dioxide thin film on NO₂ gas sensing. *J Phys Conf Ser* 1879(No. 3):032061. <https://doi.org/10.1088/1742-6596/1879/3/032061> MayIOP Publishing.
- Sta I, Jlassi M, Hajji M, Boujmil MF, Jerbi R, Kandyla M, Ezzaouia H (2014) Structural and optical properties of TiO₂ thin films prepared by spin coating. *J Sol-Gel Sci Technol* 72:421–427. <https://doi.org/10.1007/s10971-014-3452-z>.
- A. K. M. Muaz et al., “TiO₂ anatase phase structure growth, morphological optical and electrical characterization by different alcoholic solvents,” 2015 IEEE Regional Symposium on Micro and Nanoelectronics (RSM), Kuala Terengganu, Malaysia, 2015, pp. 1. <https://doi.org/10.1109/RSM.2015.7355038>.
- Salman SH, Shihab AA, Kh. Elttayef A-H (2019) “Studying the Effect of the Type of Substrate on the Structural, Morphology and Optical Properties of TiO₂ Thin Films Prepared by RF Magnetron Sputtering”. *J Energy Procedia* 157:199–207. <https://doi.org/10.1016/j.egypro.2018.11.181>.
- Ma C, Liang G, Zhu Y, Mu H, Xia F (2014) Preparation and corrosion assessment of electrodeposited Ni–SiC composite thin films. *Ceram Int* 40(2):3341–3346. <https://doi.org/10.1016/j.ceramint.2013.09.100>.
- Arunanathan MV, Selvaraj D, Natarajan P (2019) Synthesis and electrochemical studies on Cu-TiO₂ thin films deposited by spray pyrolysis technique for sensing Uric acid. *Int J Nano Dim* 10(3):230–241. 20.1001.1.20088868.2019.10.3.1.6.
- Perednis D, Gauckler LJ (2005) Thin film deposition using spray pyrolysis. *J Electroceram* 14:103–111. <https://doi.org/10.1007/s10832-005-0870-x>.
- Patil PS (1999) Versatility of chemical spray pyrolysis technique. *Mater Chem Phys* 59(3):185–198. [https://doi.org/10.1016/S0254-0584\(99\)00049-8](https://doi.org/10.1016/S0254-0584(99)00049-8).
- Dutta P, Mondal I, Saha A, Singh AK (2024) Complementary electrochromic device via a scalable solution process: a step towards affordable and energy-efficient smart windows. *J Mater Chem C* 12(30):11446–11457. <https://doi.org/10.1039/D4TC02236J>.
- Shamala KS, Vishwas M (2022) Influence of substrate temperature on optical, structural and dielectric properties of TiO₂ thin films prepared by spray pyrolysis technique. *Mater Today Proc* 52:1344–1347. <https://doi.org/10.1016/j.matpr.2021.11.071>.
- Kern W (1970) Cleaning solution based on hydrogen peroxide for use in silicon semiconductor technology. *RCA Rev* 31(2):187–206.
- Beyraghi N, Sahiner MC, Oguz O, Yerci S (2024) Optimization of a Solution-Processed TiOx/(n) c-Si Electron-Selective Interface by Pre-and Postdeposition Treatments. *ACS Appl Mater Interfaces* 16(13):16950–16961. <https://doi.org/10.1021/acsami.3c18134>.
- Wang B, Qi H, Wang H, Cui Y, Zhao J, Guo J, Shao J (2015) Morphology, structure and optical properties in TiO₂ nanostructured films annealed at various temperatures. *Opt Mater Express* 5(6):1410–1418. <https://doi.org/10.1364/OME.5.001410>.
- Gas Sensors, Editor(s): Roger Narayan, *Encyclopedia of Sensors and Biosensors (First Edition)*, Elsevier, 2023, Pages 185-208. <https://www.sciencedirect.com/science/article/pii/B9780128225486001138>.
- Witit-anun N, Kasemanankul P, Chaiyakun S, Limsuwan P (2009) Structures and optical properties of TiO₂ thin films deposited on unheated substrate by DC reactive magnetron sputtering. *Agric Nat Resour* 43(5):340–346. <https://li01.tci-thaijo.org/index.php/anres/article/view/244839>.
- Gürakar S, Ot H, Horzum S, Serin T (2020) Variation of structural and optical properties of TiO₂ films prepared by DC magnetron sputtering method with annealing temperature. *Mater Sci Eng B* 262:114782. <https://doi.org/10.1016/j.mseb.2020.114782>.

24. Pansila P, Witit-Anun N, Chaiyakun S (2012) Influence of sputtering power on structure and photocatalyst properties of DC magnetron sputtered TiO₂ thin film. *Proc Eng* 32:862–867. <https://doi.org/10.1016/j.proeng.2012.02.024>.
25. Navrotsky A (2003) Energetics of nanoparticle oxides: interplay between surface energy and polymorphism. *Geochem Trans* 4:1–4. <https://doi.org/10.1186/1467-4866-4-34>.
26. Lazzeri M, Vittadini A, Selloni A (2001) Structure and energetics of stoichiometric TiO₂ anatase surfaces. *Phys Rev B* 63(15):155409. <https://doi.org/10.1103/PhysRevB.63.155409>.
27. Nie X, Zhuo S, Maeng G, Sohlberg K (2009) Doping of TiO₂ polymorphs for altered optical and photocatalytic properties. *Int J Photoenergy* 2009(1):294042. <https://doi.org/10.1155/2009/294042>.
28. Abbas QA, Alhelaly MT, Hameed MA (2024) The inter-planner parameter and the blue shift of band gap of titanium dioxide thin films prepared using the DC reactive magnetron sputtering. *J Opt* 53(2):1516–1527. <https://doi.org/10.1007/s12596-023-01275-x>.
29. Hariyanto B, Wardani DAP, Kurniawati N, Har NP, Darmawan N (2021) X-ray peak profile analysis of silica by Williamson–Hall and size-strain plot methods. *J Phys: Conf Ser* 2019(No. 1):012106. <https://doi.org/10.1088/1742-6596/2019/1/012106>.
30. Bakri, A. S., Sahdan, M. Z., Adriyanto, F., Raship, N. A., Said, N. D. M., Abdullah, S. A., & Rahim, M. S. (2017, January). Effect of annealing temperature of titanium dioxide thin films on structural and electrical properties. In AIP conference proceedings (Vol. 1788, No. 1). AIP Publishing. <https://doi.org/10.1063/1.4968283>.
31. Kim SY, Saqlain S, Cha BJ, Zhao S, Seo HO, Kim YD (2020) Annealing temperature-dependent effects of Fe-Loading on the visible light-driven photocatalytic activity of rutile TiO₂ nanoparticles and their applicability for air purification. *Catalysts* 10(7):739. <https://doi.org/10.3390/catal10070739>.
32. Zhu L, Lu Q, Lv L, Wang Y, Hu Y, Deng Z, Teng F (2017) Ligand-free rutile and anatase TiO₂ nanocrystals as electron extraction layers for high performance inverted polymer solar cells. *RSC Adv* 7(33):20084–20092. <https://doi.org/10.1039/C7RA00134G>.
33. Wang S, Lian JS, Zheng WT, Jiang Q (2012) Photocatalytic property of Fe doped anatase and rutile TiO₂ nanocrystal particles prepared by sol–gel technique. *Appl Surf Sci* 263:260–265. <https://doi.org/10.1016/j.apsusc.2012.09.040>.
34. C.D. Wagner, W.M. Riggs, L.E. Davis, J.F. Moulder, G.E. Muilenberg, *Handbook of X-Ray Photoelectron Spectroscopy*, Perkin Elmer Corp, Publishers, Eden Prairie, MN, 1979, p. 68.
35. Potlog T, Dumitriu P, Dobromir M, Luca D (2014) XRD and XPS analysis of TiO₂ thin films annealed in different environments. *J Mater Sci Eng B* 4(6B):163–170. <https://doi.org/10.17265/2161-6221/2014.06.004>.
36. Chen S, Xiao Y, Wang Y, Hu Z, Zhao H, Xie W (2018) A facile approach to prepare black TiO₂ with oxygen vacancy for enhancing photocatalytic activity. *Nanomaterials* 8(4):245. <https://doi.org/10.3390/nano8040245>.
37. Dwivedi C, Srivastava S, Kumar A, Singh P (2025) Role of oxygen vacancies in improving the NO₂ gas sensing behavior of DC magnetron sputtered sub-stoichiometric WO₃ thin films. *Phys Scr* 100(2):025928. <https://doi.org/10.1088/1402-4896/ada311>.
38. Lopez T, Gomez R, Sanchez E, Tzompantzi F, Vera L (2001) ‘Amorphous sol-gel titania modified with heteropolyacids’. *J Sol-Gel Sci Tech* 22(Nos. 1–2):99–107. <https://doi.org/10.1007/s10971-005-6627-9>.
39. Chen YF, Lee CY, Yeng MY, Chiu HT (2003) The effect of calcination temperature on the crystallinity of TiO₂ nanopowders. *J Cryst Growth* 247(3–4):363–370. [https://doi.org/10.1016/S0022-0248\(02\)01938-3](https://doi.org/10.1016/S0022-0248(02)01938-3).
40. Suresh C, Biju V, Mukundan P, Warriar KGK (1998) Anatase to rutile transformation in sol-gel titania by modification of precursor. *Polyhedron* 17(18):3131–3135. [https://doi.org/10.1016/S0277-5387\(98\)00077-1](https://doi.org/10.1016/S0277-5387(98)00077-1).
41. Xu Y, Shen M (2008) Fabrication of anatase-type TiO₂ films by reactive pulsed laser deposition for photocatalyst application. *J Mater Process Technol* 202(1–3):301–306. <https://doi.org/10.1016/j.jmatprotec.2007.09.015>.
42. Zhang JY, Boyd IW, O’sullivan BJ, Hurley PK, Kelly PV, Senateur JP (2002) Nanocrystalline TiO₂ films studied by optical, XRD and FTIR spectroscopy. *J Non-Crystalline Solids* 303(1):134–138. [https://doi.org/10.1016/S0022-3093\(02\)00973-0](https://doi.org/10.1016/S0022-3093(02)00973-0).
43. Syed M, Gibson J, DeAnthony W, Watson D, Hamada Y, Syed M, Ahmadi T. S(2019) Effects of annealing temperature on anatase-rutile TiO₂ multilayer thin films prepared by sol-gel spin coating method. *Int J Sci Res Eng Dev* 2(6):8–18.
44. Orendorz A, Brodyanski A, Lösch J, Bai LH, Chen ZH, Le YK, Gnaser H (2007) Phase transformation and particle growth in nanocrystalline anatase TiO₂ films analyzed by X-ray diffraction and Raman spectroscopy. *Surf Sci* 601(18):4390–4394. <https://doi.org/10.1016/j.susc.2007.04.127>.
45. Mazza T, Barborini E, Piseri P, Milani P, Cattaneo D, Li Bassi A, Ducati C (2007) Raman spectroscopy characterization of TiO₂ rutile nanocrystals. *Phys Rev B-Condens Matter Mater Phys* 75(4):045416. <https://doi.org/10.1103/PhysRevB.75.045416>.
46. Lin CP, Chen H, Nakaruk A, Koshy P, Sorrell CC (2013) Effect of annealing temperature on the photocatalytic activity of TiO₂ thin films. *Energy Procedia* 34:627–636. <https://doi.org/10.1016/j.egypro.2013.06.794>.
47. Houmar M, Riassetto D, Roussel F, Bourgeois A, Berthome G, Joud JC, Langlet M (2007) Morphology and natural wettability properties of sol–gel derived TiO₂–SiO₂ composite thin films. *Appl Surf Sci* 254(5):1405–1414. <https://doi.org/10.1016/j.apsusc.2007.06.072>.
48. Mathews NR, Morales ER, Cortés-Jacome MA, Antonio JT (2009) TiO₂ thin films—Influence of annealing temperature on structural, optical and photocatalytic properties. *Sol Energy* 83(9):1499–1508. <https://doi.org/10.1016/j.solener.2009.04.008>.
49. Ying D, Zhong T (2024) Effects of thickness and annealing on the residual stress of TiO₂ film. *Opt Contin* 3(3):287–295. <https://doi.org/10.1364/OPTCON.506007>.
50. Lukong VT, Mouchou RT, Enebe GC, Ukoba K, Jen TC (2022) Deposition and characterization of self-cleaning TiO₂ thin films for photovoltaic application. *Mater Today Proc* 62:S63–S72. <https://doi.org/10.1016/j.matpr.2022.02.089>.
51. Ahmed NM, Sabah FA, Abdulgafour HI, Alsadig A, Sulieman A, Alkhoaaryef M (2019) The effect of post annealing temperature on grain size of indium-tin-oxide for optical and electrical properties improvement. *Results Phys* 13:102159. <https://doi.org/10.1016/j.rinp.2019.102159>.
52. Xu C, Tamaki J, Miura N, Yamazoe N (1991) Grain size effects on gas sensitivity of porous SnO₂-based elements. *Sens Actuators B Chem* 3(2):147–155. [https://doi.org/10.1016/0925-4005\(91\)80207-Z](https://doi.org/10.1016/0925-4005(91)80207-Z).
53. Jung D, Hwang S, Kim HJ, Han JH, Lee HN (2022) Characterization of porous CuO films for H₂S gas sensors. *Materials* 15(20):7270. <https://doi.org/10.3390/ma15207270>.
54. Li, X., Fu, L., Karimi-Maleh, H., Chen, F., & Zhao, S. (2024). Innovations in WO₃ gas sensors: Nanostructure engineering, functionalization, and future perspectives. *Heliyon*. <https://doi.org/10.1016/j.heliyon.2024.e27740>.
55. Watanabe, Y., Muramoto, Y., & Shimizu, N. (2011, October). Electronic conduction properties of TiO₂ thin films under UV light irradiation. In 2011 Annual Report Conference on Electrical Insulation and Dielectric Phenomena (pp. 117–120). IEEE. <https://doi.org/10.1109/CEIDP.2011.6232610>.
56. Baturay S, Bicer O, Yigit Gezgin S, Candan I, Budak Gumgum H, Kilic HS (2023) Influence of Mn doping on electrical properties of

- TiO₂/Si heterojunction diode. *Z für Naturforsch A* 78(6):563–578. <https://doi.org/10.1515/zna-2023-0015>.
57. Higgins JS, Shinde SR, Ogale SB, Venkatesan T, Greene RL (2004) Hall effect in cobalt-doped TiO₂– δ . *Phys Rev B* 69(7):073201. <https://doi.org/10.1103/PhysRevB.69.073201>.
 58. Ananthakumar R, Subramanian B, Yugeswaran S, Jayachandran M (2012) Effect of substrate temperature on structural, morphological and optical properties of crystalline titanium dioxide films prepared by DC reactive magnetron sputtering. *J Mater Sci: Mater Electron* 23:1898–1904. <https://doi.org/10.1007/s10854-012-0681-1>.
 59. Tian X, Hu Z, Wang T, Wang H, Zhang Q, Wei X (2023) Influence of multi-layer TiO₂/SnO₂ heterojunctions on fast and sensitive ethanol detection. *Vacuum* 207:111620. <https://doi.org/10.1016/j.vacuum.2022.111620>.
 60. Meng FJ, Xin RF, Li SX (2022) Metal oxide heterostructures for improving gas sensing properties: a review. *Materials* 16(1):263. <https://doi.org/10.3390/ma16010263>.
 61. Sivachandiran L, Thevenet F, Rousseau A, Bianchi D (2016) NO₂ adsorption mechanism on TiO₂: An in-situ transmission infrared spectroscopy study. *Appl Catal B Environ* 198:411–419. <https://doi.org/10.1016/j.apcatb.2016.05.065>.
 62. Esmaeilzadeh J, Marzbanrad E, Zamani C, Raissi B (2012) Fabrication of undoped-TiO₂ nanostructure-based NO₂ high temperature gas sensor using low frequency AC electrophoretic deposition method. *Sens Actuators B Chem* 161(1):401–405. <https://doi.org/10.1016/j.snb.2011.10.051>.
 63. Alam MW, Pooja P, Aamir M, Souayah B, Mushtaq S, Khan MS, Shajahan S (2022) The recent development in chemoresistive-based heterostructure gas sensor technology, their future opportunities and challenges: A review. *Membranes* 12(6):555. <https://doi.org/10.3390/membranes12060555>.
 64. Anpo M, Costentin G, Giamello E, Lauron-Pernot H, Sojka Z (2021) Characterisation and reactivity of oxygen species at the surface of metal oxides. *J Catal* 393:259–280. <https://doi.org/10.1016/j.jcat.2020.10.011>.
 65. Karthigeyan A, Gupta RP, Scharnagl K, Burgmair M, Zimmer M, Sharma SK, Eisele I (2001) Low temperature NO₂ sensitivity of nano-particulate SnO₂ film for work function sensors. *Sens Actuators B Chem* 78(1-3):69–72. [https://doi.org/10.1016/S0925-4005\(01\)00794-8](https://doi.org/10.1016/S0925-4005(01)00794-8).
 66. Yuan Z, Zhu X, Gao X, An C, Wang Z, Zuo C, Jiang Z (2024) Enhancing photocatalytic CO₂ reduction with TiO₂-based materials: Strategies, mechanisms, challenges, and perspectives. *Environ Sci Ecotechnol* 20:100368. <https://doi.org/10.1016/j.ese.2023.100368>.
 67. Raza MA, Habib A, Kanwal Z, Hussain SS, Iqbal MJ, Saleem M, Naseem S (2018) Optical CO₂ gas sensing based on TiO₂ thin films of diverse thickness decorated with silver nanoparticles. *Adv Mater Sci Eng* 2018(1):2780203. <https://doi.org/10.1155/2018/2780203>.
 68. Patil VL, Vanalakar SA, Shendage SS, Patil SP, Kamble AS, Tarwal NL, Patil PS (2019) Fabrication of nanogranular TiO₂ thin films by SILAR technique: Application for NO₂ gas sensor. *Inorg Nano-Met Chem* 49(7):191–197. <https://doi.org/10.1080/24701556.2019.1599948>.
 69. Müller JO, Frank B, Jentoft RE, Schlögl R, Su DS (2012) The oxidation of soot particulate in the presence of NO₂. *Catal Today* 191(1):106–111. <https://doi.org/10.1016/j.cattod.2012.03.010>.
 70. Bak SY, Lee J, Kim Y, Lee SH, Woo K, Lee S, Yi M (2019) Sensitivity Improvement of Urchin-Like ZnO Nanostructures Using Two-Dimensional Electron Gas in MgZnO/ZnO. *Sensors* 19(23):5195. <https://doi.org/10.3390/s19235195>.
 71. Noh J, Kwon SH, Park S, Kim KK, Yoon YJ (2021) TiO₂ nanorods and Pt nanoparticles under a UV-LED for an NO₂ gas sensor at room temperature. *Sensors* 21(5):1826. <https://doi.org/10.3390/s21051826>.
 72. Mohammadi MR, Fray DJ (2007) Semiconductor TiO₂–Ga₂O₃ thin film gas sensors derived from particulate sol–gel route. *Acta Mater* 55(13):4455–4466. <https://doi.org/10.1016/j.actamat.2007.04.011>.
 73. Ramgir N, Bhusari R, Rawat NS, Patil SJ, Debnath AK, Gadkari SC, Muthe KP (2020) TiO₂/ZnO heterostructure nanowire based NO₂ sensor. *Mater Sci Semiconductor Process* 106:104770. <https://doi.org/10.1016/j.mssp.2019.104770>.
 74. Sharma A, Tomar M, Gupta V (2013) Enhanced response characteristics of SnO₂ thin film based NO₂ gas sensor integrated with nanoscaled metal oxide clusters. *Sens Actuators B Chem* 181:735–742. <https://doi.org/10.1016/j.snb.2013.01.074>.
 75. Tan J, Wlodarski W, Kalantar-Zadeh K (2007) Nitrogen dioxide gas sensors based on titanium dioxide thin films deposited on langasite. *Thin Solid Films* 515(24):8738–8743. <https://doi.org/10.1016/j.tsf.2007.04.008>.
 76. Zampetti E, Pantalei S, Muzyczuk A, Bearzotti A, De Cesare F, Spinella C, Macagnano A (2013) A high sensitive NO₂ gas sensor based on PEDOT–PSS/TiO₂ nanofibres. *Sens Actuators B Chem* 176:390–398. <https://doi.org/10.1016/j.snb.2012.10.005>.
 77. Gönüllü Y, Haidry AA, Saruhan B (2015) Nanotubular Cr-doped TiO₂ for use as high-temperature NO₂ gas sensor. *Sens Actuators B Chem* 217:78–87. <https://doi.org/10.1016/j.snb.2014.11.065>.
 78. Yeh YM, Chang SJ, Fang SY, Hsueh TJ (2024) TiO₂-based nitrogen dioxide gas sensor with transparent ordered micro-hollow bump structure prepared by 3D heterogeneous integration technology. *Mater Sci Semiconductor Process* 184:108832. <https://doi.org/10.1016/j.mssp.2024.108832>.
 79. Bharathi P, Harish S, Shimomura M, Mohan MK, Archana J, Navaneethan M (2024) Ultrasensitive and reversible NO₂ gas sensor based on SnS₂/TiO₂ heterostructures for room temperature applications. *Chemosphere* 346:140486. <https://doi.org/10.1016/j.chemosphere.2023.140486>.
 80. Francioso L, Forleo A, Capone S, Epifani M, Taurino AM, Siciliano P (2006) Nanostructured In₂O₃–SnO₂ sol–gel thin film as material for NO₂ detection. *Sens Actuators B: Chem* 114(2):646–655. <https://doi.org/10.1016/j.snb.2005.03.124>.

Publisher's note Springer Nature remains neutral with regard to jurisdictional claims in published maps and institutional affiliations.

Springer Nature or its licensor (e.g. a society or other partner) holds exclusive rights to this article under a publishing agreement with the author(s) or other rightsholder(s); author self-archiving of the accepted manuscript version of this article is solely governed by the terms of such publishing agreement and applicable law.